



CrossMark
click for updates

Cite this: *Nanoscale*, 2014, 6, 10370

Carbon coated face-centered cubic Ru–C nanoalloys†

Zhisheng Zhao,^{‡,ad} Chuanmin Meng,^{‡,b} Peifang Li,^{§,c} Wenjun Zhu,^b Qianqian Wang,^a Yanming Ma,^c Guoyin Shen,^d Ligang Bai,^d Hongliang He,^b Duanwei He,^e Dongli Yu,^a Julong He,^a Bo Xu^{*a} and Yongjun Tian^a

Carbon-encapsulated ruthenium–carbon (Ru–C) nanoalloys were synthesized by dynamic shocks. The Ru–C alloy shows a new fcc structure different from the original hcp structure of metal Ru. This fcc phase is assigned to a Ru₃₂C₄ solid solution with a lattice parameter of 3.868(2) Å and a bulk modulus K_{T0} of 272(12) GPa. The small amount of carbon in the solid solution enhances the thermodynamic and chemical stabilities with respect to pure Ru, as well as induces changes in the electronic properties, which have direct applications in improving the material's catalytic activity and selectivity.

Received 14th May 2014
Accepted 27th June 2014

DOI: 10.1039/c4nr02632b

www.rsc.org/nanoscale

1. Introduction

Ruthenium (Ru) and its alloys are important chemical catalysts and have been widely used in multi-purpose applications, such as hydrogenation, isomerization, oxidation, and reforming reactions.^{1–4} Possible pathways to improve the catalytic activity and conversion efficiency of this class of catalysts include changes of morphology, structure, and composition, as well as the use of various carbon forms as carriers. At present, controlling the size and shape by different synthesis approaches has been extensively studied. However, research on new structures and compositions is rare, and the understanding of the interaction between carbon and noble-metal catalysts has not been well established.

Pressure, together with temperature and nanoscale effects, provides a wider dimension to study a material's behavior. Metal elements usually display polymorphism when subjected to high pressure.⁵ However, Ru was found to possess only a hexagonal close-packed (hcp) structure up to 56 GPa at room temperature.⁶ Recently, a new face-centered cubic (fcc) Ru

nanophase with diameters of less than 6 nm was synthesized by the chemical reduction method. The fcc-Ru showed significant chemical activity.^{7,8} In order to further improve the thermodynamic and chemical stability of a parent phase, alloying is usually applied. One successful example is Ru–Pt alloy, which is widely applied as a CO-tolerant electrocatalyst.^{1,4} Nonetheless, it is generally thought that refractory metal catalysts (*e.g.*, Ru, Rh, Pd, Pt, Ir, Re, Au, Ag) are very hard to form carbides or solid solutions with carbon. As a result, carbon is widely used as a separate carrier in catalytic metal nanoparticles to promote chemical reactions.

Herein, we conducted dynamic shock experiments on pure Ru and Ru–C mixtures. A novel solid solution alloy, fcc Ru–C, coated with carbon (core–shell structure) was observed in the recovered samples. In this paper, we report the results of structural, morphological, mechanical, and electronic characterizations, and discuss the formation mechanism of this fcc Ru–C alloy. Our results have implications for improving the physical and chemical properties, and also in the phase diagrams of refractory metals (and their alloys). It is hoped that this study will motivate further research to create exotic nano-materials with extraordinary configurations and properties.

2. Materials and methods

Shock-wave experiment

Two sets of materials, pure Ru and a Ru–C mixture with a molar ratio of 1 : 2 (Ru powder: 325 mesh and 99.9%, carbon black: 99.9+%, Alfa Aesar), were ball-milled for 50 hours in an iron milling pot with a speed of 600 rpm, and then purified with dilute sulfuric acid. The dynamic shock experiments were then conducted on the ball-milled materials respectively by employing a two-stage light gas gun and a chemical detonation system at the Institute of Fluid Physics, China Academy of Engineering

^aState Key Laboratory of Metastable Materials Science and Technology, Yanshan University, Qinhuangdao, Hebei 066004, China. E-mail: bxu@ysu.edu.cn

^bNational Key Laboratory of Shock Wave and Detonation Physics, Institute of Fluid Physics, China Academy of Engineering Physics, Mianyang, Sichuan 621900, China

^cState Key Laboratory of Superhard Materials, Jilin University, Changchun 130012, China

^dHigh Pressure Collaborative Access Team, Geophysical Laboratory, Carnegie Institution of Washington, Argonne, IL 60439, USA

^eInstitute of Atomic and Molecular Physics, Sichuan University, Chengdu 610065, China

† Electronic supplementary information (ESI) available. See DOI: 10.1039/c4nr02632b

‡ Z. Z. and C. M. contributed equally.

§ Present address: College of Physics and Electronic Information, Inner Mongolia University for the Nationalities, Tongliao, Inner Mongolia 028000, China.

Physics,^{9,10} and these are schematically illustrated in Fig. S1 in ESI.† After the impact experiments, all recovered samples (4 mm in dimension) were carefully peeled from the copper container and purified with acid. The Hugoniot parameters were taken from LASL Shock Hugoniot Data for carbon,¹¹ and calculated from the bulk modulus and its first derivative (determined in this work) for pure Ru.¹² The Hugoniot parameters of the dense and porous Ru–C mixtures were calculated according to the method given by Meyers¹³ and Batasanov,¹⁴ respectively. The shock pressure and temperature of pure Ru and Ru–C mixture samples were estimated by using the shock impedance match method¹⁵ and the thermodynamic approach,¹² respectively (see ESI† for further details of the estimation methods).

Structure and morphology characterizations

The structure, morphology, and composition of the ball-milled materials and the shock-recovered samples were characterized by multiple analysis methodologies, including X-ray diffraction (XRD, Bruker D8 Discover with Cu K α), field-emission scanning electron microscopy (SEM, Hitachi S-4800) equipped with energy dispersive X-ray spectroscopy (EDS), and transmission electron microscopy (TEM, JEOL JEM-2010) equipped with selected area electron diffraction (SAED) at Yanshan University.

High pressure X-ray diffraction

In situ high-pressure X-ray diffraction on samples up to 43.2(3) GPa were conducted at beam line 16-ID-B of the High Pressure Collaborative Access Team (HPCAT) at the Advanced Photon Source (APS), Argonne National Laboratory (ANL). The recovered Ru–C sample was loaded into a 300 μm culet diamond anvil cell (DAC) with Re as a confining gasket and neon as the pressure transmitting medium. The pressure was calibrated by fluorescence measurements of ruby spheres loaded in the sample chamber. All the structural data were collected using monochromatic synchrotron X-ray radiation ($\lambda = 0.620 \text{ \AA}$).

Corrosion experiment

The chemical stability of the recovered Ru–C nanoparticles was tested by corrosion experiments. The powders were soaked in boiling concentrated sulfuric acid for 8 hours. Then the sulfuric acid was poured out, and the powders were repeatedly washed with distilled water for further characterization.

Calculation details

Calculations for optimal structures, enthalpies, elastic constants, and electronic density of states (DOS) were carried out using the density functional theory (DFT) as implemented in the CASTEP code.¹⁶ The Vanderbilt ultrasoft pseudopotential was used with a cut-off energy of 330 eV for the plane wave basis set,¹⁷ and the covalent electrons of C $2s^2 2p^2$ and Ru $4s^2 4p^6 4d^7 5s^1$ were used for calculations. The exchange-correlation function was treated by the Perdew–Burke–Ernzerhof form of the generalized gradient approximation (GGA).¹⁸ A 0.04 \AA^{-1} separation was used to generate the k -point grid resulting from

the Monkhorst-Pack method.¹⁹ Structural relaxation was performed until the energy change per atom was less than 5×10^{-6} eV, the forces on atoms were less than 0.01 eV \AA^{-1} , and all the stress components were less than 0.02 GPa. Mulliken overlap populations were integrated with a cut-off distance of 3 \AA . Because the GGA calculation can slightly overestimate the atomic volume, the simulated lattice parameters of the considered phases were recalibrated by a criterion of eliminating the deviation between the calculated and experimental values of hcp Ru.

In order to compare electronic changes between bulk and surface structures, the hcp Ru (0001) clean surface model was built by stacking two-dimensional (0001) crystal planes with a thickness of 6 atomic layers cleaved from the $3 \times 3 \times 3$ supercell of the hcp Ru crystal. On the top of the surface, a vacuum slab of 1.5 nm was added to avoid mirror interactions occurring. The atoms of the top two layers were free to relax, in order to simulate the surface state, while the atomic fractional positions of the lower four layers were fixed to maintain the bulk environment. The constructions of fcc Ru and Ru₃₂C₄ (111) surfaces were performed in a similar procedure as hcp Ru (0001). All the surface structure models are presented in Fig. S2 of ESI.† The pressure–temperature (P – T) phase diagram of Ru was explored using a quasi-harmonic approximation,²⁰ and the finite-temperature hcp–fcc and solid–liquid (melting points) phase boundaries were also determined. The phase transition paths were simulated using the variable-cell nudged elastic band (VC-NEB) method.²¹

3. Results and discussion

Structure and morphology characterization

For pure Ru, XRD patterns of both ball-milled and shock-recovered samples showed identical hcp structures, although much sharper diffraction peaks appeared in the recovered sample, indicating a high degree of crystallinity and relatively larger grains after the dynamic shock (Fig. S3 of ESI.†). SEM observations (Fig. S4 of ESI.†) indicated that the milled spheroidal Ru particles merged into the bulk after the shock impacts, with grain boundaries and micropores also apparent. Interestingly, new peaks in addition to those from the hcp phase were observed in the recovered Ru–C mixture, as shown in Fig. 1 and S5 of ESI,† which can be attributed to an fcc phase with an ambient-pressure lattice parameter of $3.868(2) \text{ \AA}$. SEM observations revealed the formation of a large number of spherical particles with a size distribution from several nanometers to hundreds of nanometers in the recovered Ru–C mixture, as shown in Fig. S4 of ESI† and Fig. 2a. In addition, sintered metal aggregations similar to those observed in the shocked-recovered pure Ru sample of hcp structure were observed in the quenched Ru–C sample. The spherical particles were identified to the carbon encapsulated core–shell structure according to the TEM analysis (Fig. 2b). The SAED measurements on these carbon-coated particles with sizes less than 50 nm showed a square diffraction pattern (Fig. S6 of ESI.†). These spots can be attributed to the $\{200\}$ diffraction from an fcc structure with an interplanar spacing of $1.934(5) \text{ \AA}$, which is

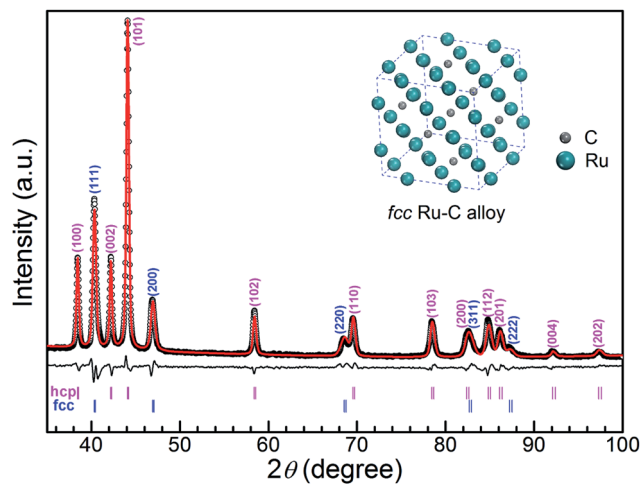


Fig. 1 XRD patterns of the shock-recovered Ru–C mixture (ground powders) at ambient conditions. The difference between the observed (black circles) and Rietveld refinement fitted (red line) diffraction pattern is shown as the black line. Bragg positions of hcp Ru and fcc Ru–C phases are marked with vertical tags. Cu $K\alpha$ of 1.542 Å was employed in the XRD measurement. The inset shows the crystal structure of the fcc Ru–C alloy.

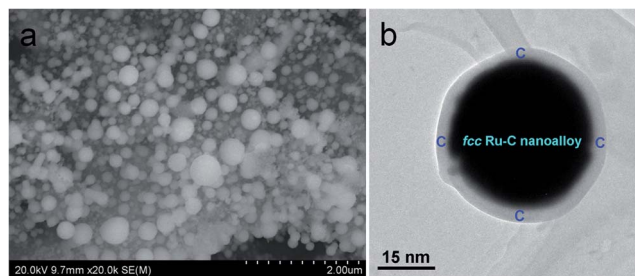


Fig. 2 (a) SEM image of a recovered Ru–C mixture bulk sample. (b) TEM image of fcc Ru–C nanoalloy after the dynamic shock experiment.

consistent with the XRD results. It should be mentioned that attempts to check the crystal structure for larger carbon-coated particles were unsuccessful due to the intensive electron absorption of Ru.

The new peaks in the XRD patterns of the recovered Ru–C mixture are attributed to an fcc structure with a stacking sequence of ABC. Other possible stacking sequences for this new phase have also been checked by comparing the simulated

and experimental XRD patterns, such as the double hexagonal close-packed (dhcp) structure with ABAC stacking sequence (Fig. S7 of ESI†). The absence of a superlattice reflection, *i.e.*, the (103) peak from the dhcp structure, and the inconsistency of some diffraction peaks exclude candidates other than the fcc structure. Hence, the quenched Ru–C product must be a mixture of hcp Ru and an fcc phase. The Rietveld refinement gives the lattice parameters listed in Table 1 for the raw and shock-quenched materials.

Carbon in the fcc crystal lattice

The next problem to be clarified is the role of carbon in the fcc phase in the shock-quenched Ru–C samples. The room temperature pressure–volume (P – V) relationships of hcp Ru and the fcc phase in the shock-recovered Ru–C sample are shown in Fig. 3, which were deduced from synchrotron XRD measurements (Fig. S8 of ESI†). Due to the same atomic packing factor of 0.74 and coordination number of 12, fcc and hcp Ru structures should have close atomic volumes. However, the experimentally determined average atomic volume of Ru in the fcc phase (a quarter of the refined unit cell volume) is *ca.* 1 Å³ per Ru atom larger than that of hcp Ru (half of the refined unit cell volume) at ambient and high pressure (Fig. 3). Since the experimental determined lattice parameters of hcp Ru agree well among all samples in this study and are consistent with the calculated values as well, the lattice expansion in the fcc phase can be accounted for by carbon atoms dissolving into interstitial sites of Ru fcc lattice to form a Ru–C alloy. This argument is further supported by the crystal lattice distortion indicated in the SAED pattern (Fig. S6 of ESI†).

In an fcc structure, the size of the octahedral interstitial sites is larger than that of the tetragonal interstitial sites. Carbon atoms thus most likely occupy the octahedral sites. Based on the octahedral-space-occupancy accommodation of carbon atoms, we built fcc supercells with 32 Ru atoms and variable numbers of carbon atoms to simulate a series of Ru–C alloys (Ru₃₂C, Ru₃₂C₂...Ru₃₂C₈). The calculated average Ru atomic volume increased monotonically with increasing carbon content and decreases with increasing pressure. The best match was achieved at a composition of Ru₃₂C₄, as demonstrated in Fig. 3. We note that the diameters of the octahedral interstitial sites in hcp- and fcc-structured Ru are both 0.111 nm as calculated from the hard sphere model, which are smaller than that of carbon atom (0.154 nm). Lattice distortion and expansion would be expected after the carbon atom dissolving, as indicated by the experimental observations.

Table 1 Lattice parameters of hcp Ru and fcc Ru–C alloy at ambient conditions from Rietveld refinement. The reliability parameters are: R_w , weighted profile factor; R_B , Bragg factor; R_{exp} , expected factor

Sample	Phase	Symmetry	Atomic position	a (Å)	c (Å)	R_w (%)	R_B (%)	R_{exp} (%)
Ball-milled Ru	hcp	$P6_3/mmc$	$2c$ (1/3,2/3,1/4)	2.705(2)	4.282(2)	6.91	5.47	9.62
Recovered Ru	hcp	$P6_3/mmc$	$2c$ (1/3,2/3,1/4)	2.702(3)	4.280(3)	8.65	5.32	7.65
Ball-milled Ru–C mixture	hcp	$P6_3/mmc$	$2c$ (1/3,2/3,1/4)	2.705(2)	4.279(2)	8.07	5.58	8.43
Recovered Ru–C mixture	hcp	$P6_3/mmc$	$2c$ (1/3,2/3,1/4)	2.703(3)	4.280(2)	7.06	5.54	5.44
	fcc	$Fm\bar{3}m$	$4a$ (0,0,0)	3.868(2)				

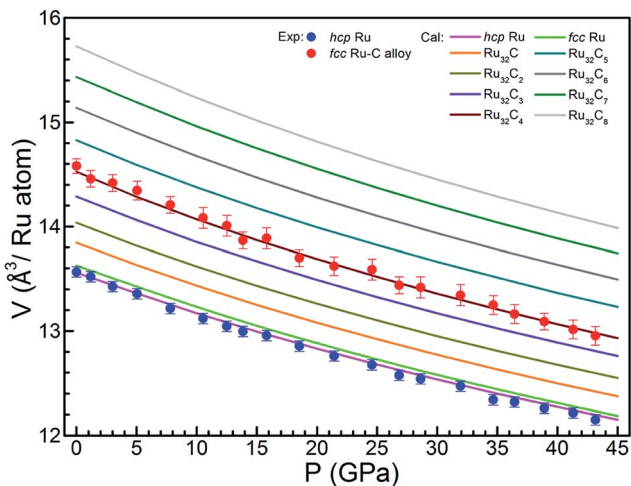


Fig. 3 Pressure–volume relationships for hcp Ru, fcc Ru–C, and a series of fcc Ru–C alloys. The experimental and simulated data are presented with solid circles and lines, respectively. See text for more details.

Formation mechanism

To gain insights into the formation mechanism, we calculated the P – T phase diagram of Ru, which clearly displayed a narrow stable region of fcc Ru over hcp Ru below the melting curve, as shown in Fig. 4. Our calculations reveal that fcc Ru has a higher energy of 113 meV per atom at ambient pressure than that of hcp Ru, which is consistent with the 136 meV per atom reported previously.²² The existence of an fcc phase at high temperature provides a clue for a possible formation mechanism. During the dynamic shocks at high pressures (40–70 GPa) and high temperatures (3000–5000 K), Ru enters the fcc-phase stable region and changes its structure from hcp to fcc at such

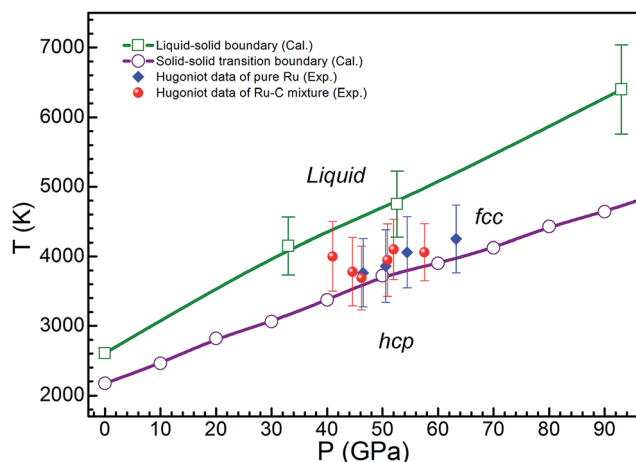


Fig. 4 Pressure–temperature phase diagram of Ru. The blue diamonds and red points show the estimated Hugoniot shock states for pure Ru and for the Ru–C mixture, respectively. The lines with open circles and squares show the predicted hcp–fcc and fcc–liquid transition boundaries, respectively. The lines are included as guides for the eyes.

conditions (Fig. 4). However, this fcc structure would be unstable and changes back to the hcp structure at low pressure and temperature. This is consistent with our shock experiments on pure Ru, where Ru recrystallized into hcp bulk, with large grains clearly observed (Fig. S3 and S4†). In comparison, fcc Ru–C nanoalloys were found in the shock-recovered Ru–C mixture, along with hcp Ru. It should be noted that the existence of an hcp Ru–C alloy is excluded by the identical lattice parameters of hcp Ru from both the ball-milled powders and the shock-recovered samples (Table 1).

To clarify this obvious difference, we theoretically investigated the hcp–fcc phase transition under high pressure using the VC-NEB method.²¹ The phase transition involves atomic slips, inducing lattice distortion and readjustment of the interstitial sites, as shown in Fig. 5. During the transition process, the hcp structure undergoes a lattice stretch and contraction (see the arrows in Fig. 5b), the octahedral interstitial sites in the hcp structure (marked as the red octahedron) is squashed and eliminated with the formation of octahedral interstitial sites in the fcc structure (blue octahedron), and eventually the fcc structure is achieved. Without carbon, the transition process is reversible and an fcc Ru cannot be quenched to ambient conditions. However, if carbon atoms are present, they have a chance to enter the opening octahedral interstitial sites of the intermediate distorted fcc phase (Fig. 5c) during this process. Once carbon atoms enter the fcc lattice, they increase the resistance to atomic motions such that slips back to the hcp structure are difficult to occur. Consequently, fcc Ru–C alloy can be recovered to ambient conditions. Carbon dissolution thus increases the stability of the Ru fcc structure. This is similar to the stability of fcc γ -Fe and fcc Fe–C alloys (common steel materials). The pure fcc γ -Fe is only thermodynamically stable at high temperatures,²³ and cannot be quenched to ambient conditions. Alloying with certain

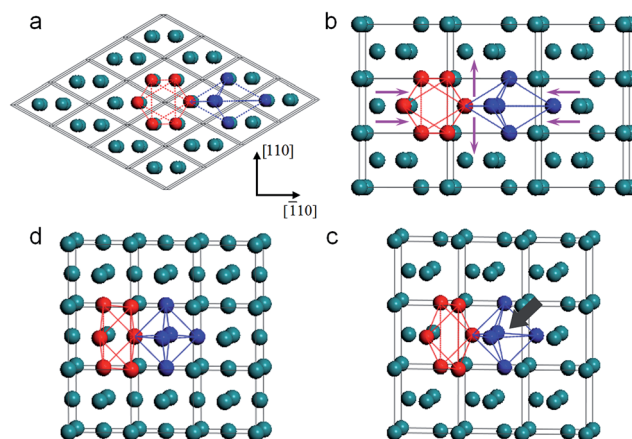


Fig. 5 Structural evolution from hcp Ru to fcc Ru at high pressure. (a) hcp Ru with ordinary unit cells. (b) hcp Ru with unit cells redrawn along [110] and $\bar{[110]}$ directions of (a). The purple arrows indicate the directions of lattice stretch and contraction during the transition process. (c) An intermediate state between hcp and fcc phases. The gray arrow signals the filling of the carbon atom. (d) fcc Ru.

elements (*e.g.*, C and Mn) stabilizes the fcc structure at room temperature.

It should be noted that our calculations were performed without considering the nanosize effect. For small Ru nano-clusters with 55 and 135 atoms, the icosahedron geometries were predicted to be more stable than the cubo-octahedral (fcc) geometries.²⁴ However, energy comparisons for larger clusters with 140 atom ($\phi \approx 1.2$ nm) reverse the stability order, with the fcc configuration favored over the icosahedron one.²⁴ Moreover, larger surface relaxations were found in the fcc structure, where unique reactive properties in surfaces may be expected.²⁴

Electronic and mechanical properties

The structural change, as well as interstitial atoms, can induce significant modifications in the bulk and surface electronic structures, and lead to distinctive catalytic activities and selectivity. We checked the density of states (DOS), Mulliken populations, Hirshfeld charges, and bond lengths of the pure Ru and the Ru–C alloy with bulk and surface models. The calculated DOS are presented in Fig. 6 (hcp Ru and fcc Ru–C alloy) and Fig. S9 of ESI† (fcc Ru). Other results are summarized in

Table S1 of ESI.† Obviously for all systems, there are more active electrons at the Fermi level in surface structures than those in bulks, explaining the stronger catalytic activity of the surface. Also, the (111) surfaces of the fcc Ru–C alloy and fcc Ru are apparently more active than that of the (0001) surface of hcp Ru traditionally used in the chemical reaction. This increased metallic character in DOS near the Fermi level mainly originates from the higher electron occupations in Ru d-band, which is also believed to give rise to some similarities in the catalytic properties of other transition metal–carbon alloys (*e.g.* Mo–C and W–C alloys) and noble metals (Pt and Ru).^{25,26} Notably, previous experiments have demonstrated that large fcc Ru nanoparticles are more reactive in CO oxidation than hcp Ru nanoparticles.^{7,27} Because the fcc Ru–C alloy surface has a slightly higher activated electron state at the Fermi level than that of fcc Ru, more efficient chemical catalysis is expected for the fcc Ru–C alloy.

In addition to the DOS differences, Hirshfeld charge analyses showed a larger variety of charged atoms in the Ru–C alloy than those in hcp and fcc Ru (Table S1†). Such variations in atomic charge states are effective for multiple adsorption and selectivity, which are important for the catalytic performance. For example, Ru atoms with different charges can easily adsorb various species such as H and CO. Our DFT calculations thus signify the advantage of the fcc Ru–C alloy as a prospective catalyst, such as its more active electrons at the Fermi level and multivalued charge states.

Compared to the changes in electronic properties, the difference of mechanical elastic properties is not as significant. The measured compression data for hcp Ru and fcc Ru–C alloy from a quenched Ru–C mixture (Fig. 3) were fitted with the third-order Birch–Murnaghan EOS, giving the ambient-pressure isothermal bulk modulus (K_{T0}) of 298(8) GPa and 272(12) GPa with the first pressure derivative ($K'_{T0} = dK_{T0}/dP$) of 5.05(0.60) and 5.27(0.82), respectively. K_{T0} of 312(4) and 289(6) GPa for hcp Ru and fcc Ru–C alloy, respectively, are deduced from the second-order Birch–Murnaghan EOS with a fixed K'_{T0} of 4. On the other hand, the elastic constants, C_{ij} , were calculated theoretically based on the stress and strain relation (Hooke's law). Then, the ambient-pressure adiabatic bulk modulus (K_{S0}) and shear modulus (G_0) for the polycrystals were estimated using the Voigt–Reuss–Hill approximation, which is the arithmetic average of the upper (Voigt) and lower (Reuss) bounds for the actual macroscopic effective elastic constants.²⁸ All the data is listed in Table 2, and both experimental and theoretical results show the close bulk moduli of hcp Ru, fcc Ru, and fcc Ru–C alloy.

Chemical stability and the role of carbon in noble metal catalysis

Common metal or alloy nanoparticles with specific volume and surface effects are usually highly activated, and sensitive to the environment conditions (*e.g.*, temperature, humidity, light, and magnetic field, *etc.*). It is challenging to protect these nanoparticles from physical and chemical changes, such as aggregation and growth, oxidation, and hydrolysis reactions. Here we

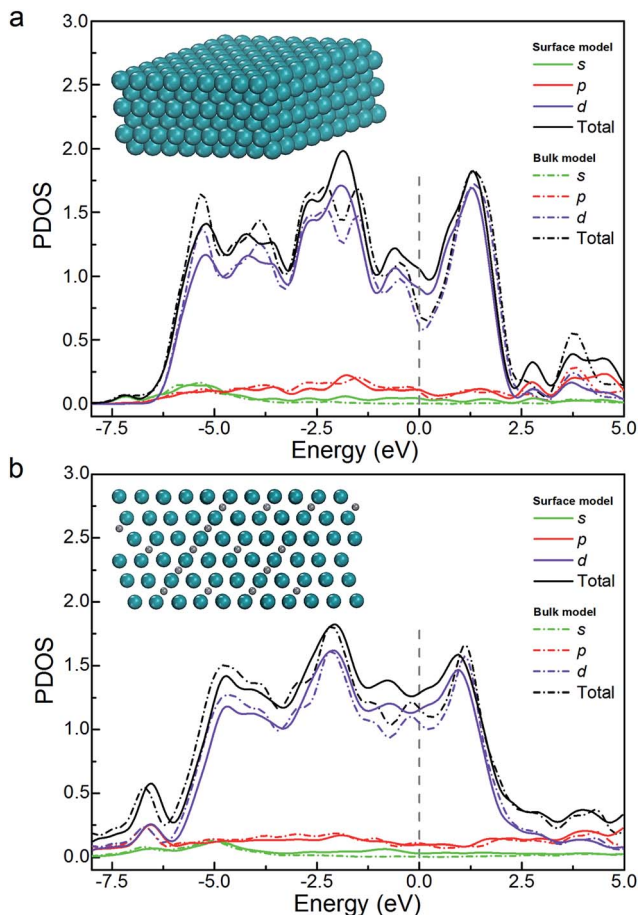


Fig. 6 Density of states (electron number per eV per atom) of different bulk and surface models. (a) hcp Ru. (b) fcc Ru–C alloy. Surface models of hcp Ru (0001) and fcc Ru₃₂C₄ (111) are shown as insets. Ru atoms and C atoms are shown in dark cyan and gray, respectively.

Table 2 Elastic constants (GPa), bulk and shear moduli (GPa), and first derivatives of the bulk modulus for hcp Ru, fcc Ru–C alloy, and fcc Ru

Phase	C_{11}	C_{33}	C_{44}	C_{12}	C_{13}	K_{S0}	G_0	K_{T0}	K'_{T0}
hcp Ru	596(5)	660(8)	202(2)	164(2)	157(3)	312(2)	215(1)	298(8)	5.05(0.60)
fcc Ru–C alloy	508(3)		175(2)	179(2)		288(2)	170(1)	312(4)	4.0
fcc Ru	478(2)		226(2)	223(1)		308(1)	179(1)	272(12)	5.27(0.82)
								289(6)	4.0

have demonstrated the advantage of the dynamic shock method for achieving a large amount of carbon-coated nanoparticles with unique configurations. These core–shell nanoparticles show superb stability as demonstrated by the long time (8 hours) corrosion experiment using boiling concentrated sulfuric acid.

The successful synthesis of the Ru–C nanoalloy may explain the previously observed anomalous electronic structure in fullerene-soot-supported Ru nanoparticles.⁴ Similar alloying behavior exists in other systems such as Pt–C,^{29,30} Pd–C,³¹ and Re–C.³² For example, a superficial PtC_x ($x \approx 1$) compound was evidenced in Pt polycrystalline films containing up to 17% carbon prepared by d.c. reactive sputtering.³³ A superlattice structure of Pt–C was proposed based on the observations of an ordered Pt₇C structure in the grain boundaries following quenching or irradiation.³⁴ The formation of a Pd₆C alloy on the Pd surface was used to account for the catalytic activity of palladium toward the selective hydrogenation of hydrocarbons.³¹ We expect current research can lead to a re-examination of the role of carbon in noble metal catalysis.

4. Conclusions

In summary, carbon-encapsulated Ru–C nanoparticles with an fcc structure have been produced by using the explosion shock method. The obviously expanded crystal lattice suggests carbon dissolution into the interstitial sites of fcc-structured Ru, which is further shown by first-principle calculations to be the Ru₃₂C₄ alloy phase. The carbon dissolution enhances the thermodynamic and chemical stability of the fcc structure, and also induces change in the mechanical and electronic properties. In particular, the increase in the activated electrons at the Fermi level and the redistribution of electric charge among atoms can significantly enhance the material's catalytic activity and selectivity.

Acknowledgements

This work is supported by National Basic Research Program of China (2011CB808205), National Science Foundation of China (51121061 and 51332005), Natural Science Foundation for Distinguished Young Scholars of Hebei Province of China (E2014203150), Science and Technology Development Foundation (Grant no. 2012B0101002), Foundation of Shuangbai of Chinese Academy of Engineering Physics (Grant no. SHUANGBAI-2011), and Foundation of National Key Laboratory of Shock Wave and Detonation Physics (Grant no.

9140C670203110C6705). HPCAT is supported by DOE-NNSA (Contract no. DE-NA0001974) and DOE-BES (Contract no. DE-FG02-99ER45775), with partial instrument support from NSF. APS is supported by DOE-BES (Contract no. DE-AC02-06CH11357). Zhisheng Zhao is partially supported by Efree, an Energy Frontier Research Center funded by DOE-BES (Award Number DE-SC0001057). We thank Guangrui Qian in Stony Brook University for the help of phase transition path calculations.

References

- 1 S. Alayoglu, A. U. Nilekar, M. Mavrikakis and B. Eichhorn, *Nat. Mater.*, 2008, **7**, 333–338.
- 2 P. Gallezot, N. Nicolaus, G. Flèche, P. Fuertes and A. Perrard, *J. Catal.*, 1998, **180**, 51–55.
- 3 B. W. Hoffer, E. Crezee, P. R. M. Mooijman, A. D. van Langeveld, F. Kapteijn and J. A. Moulijn, *Catal. Today*, 2003, **79–80**, 35–41.
- 4 C. W. Hills, M. S. Nashner, A. I. Frenkel, J. R. Shapley and R. G. Nuzzo, *Langmuir*, 1999, **15**, 690–700.
- 5 M. I. McMahon and R. J. Nelmes, *Chem. Soc. Rev.*, 2006, **35**, 943–963.
- 6 H. Cynn, J. E. Klepeis, C.-S. Yoo and D. A. Young, *Phys. Rev. Lett.*, 2002, **88**, 135701.
- 7 K. Kusada, H. Kobayashi, T. Yamamoto, S. Matsumura, N. Sumi, K. Sato, K. Nagaoka, Y. Kubota and H. Kitagawa, *J. Am. Chem. Soc.*, 2013, **135**, 5493–5496.
- 8 S. H. Joo, J. Y. Park, J. R. Renzas, D. R. Butcher, W. Huang and G. A. Somorjai, *Nano Lett.*, 2010, **10**, 2709–2713.
- 9 H. He, T. Sekine, T. Kobayashi, H. Hirosaki and I. Suzuki, *Phys. Rev. B: Condens. Matter Mater. Phys.*, 2000, **62**, 11412–11417.
- 10 H. Huang, Y. Fei, L. Cai, F. Jing, X. Hu, H. Xie, L. Zhang and Z. Gong, *Nature*, 2011, **479**, 513–516.
- 11 S. P. Marsh, *LANL Shock Hugoniot Data*, University of California Press, Ltd., Berkeley, Los Angeles, London, 1980.
- 12 F. Jing, *Introduction to Experimental Equation of State*, Science Press, Beijing, 1999.
- 13 M. A. Meyers, *Dynamic Behavior of Materials*, John Wiley & Son, INC., New York, Chichester, Brisbane, Toronto, Singapore, 1994.
- 14 S. S. Batasanov, *Effects of Explosion on Materials: Modification and Synthesis Under High-Pressure Shock Compression*, Springer-Verlag, New York, Berlin, Heidelberg, London, Paris, 1994.

- 15 A. C. Mitchell and W. J. Nellis, *J. Appl. Phys.*, 1981, **52**, 3363–3374.
- 16 S. J. Clark, M. D. Segall, C. J. Pickard, P. J. Hasnip, M. I. J. Probert, K. Refson and M. C. Payne, *Z. Kristallogr. - Cryst. Mater.*, 2005, **220**, 567–570.
- 17 D. Vanderbilt, *Phys. Rev. B: Condens. Matter Mater. Phys.*, 1990, **41**, 7892–7895.
- 18 J. P. Perdew, K. Burke and M. Ernzerhof, *Phys. Rev. Lett.*, 1996, **77**, 3865–3868.
- 19 H. J. Monkhorst and J. D. Pack, *Phys. Rev. B: Solid State*, 1976, **13**, 5188–5192.
- 20 P. Li, G. Gao, Y. Wang and Y. Ma, *J. Phys. Chem. C*, 2010, **114**, 21745–21749.
- 21 G.-R. Qian, X. Dong, X.-F. Zhou, Y. Tian, A. R. Oganov and H.-T. Wang, *Comput. Phys. Commun.*, 2013, **184**, 2111–2118.
- 22 R. E. Cohen, M. J. Mehl and D. A. Papaconstantopoulos, *Phys. Rev. B: Condens. Matter Mater. Phys.*, 1994, **50**, 14694–14697.
- 23 G. Shen, H. K. Mao, R. J. Hemley, T. S. Duffy and M. L. Rivers, *Geophys. Res. Lett.*, 1998, **25**, 373–376.
- 24 D. R. Jennison, P. A. Schultz and M. P. Sears, *J. Chem. Phys.*, 1997, **106**, 1856–1862.
- 25 S. T. Oyama, *Catal. Today*, 1992, **15**, 179–200.
- 26 J. R. Kitchin, J. K. Nørskov, M. A. Barteau and J. G. Chen, *Catal. Today*, 2005, **105**, 66–73.
- 27 K. Qadir, S. H. Joo, B. S. Mun, D. R. Butcher, J. R. Renzas, F. Aksoy, Z. Liu, G. A. Somorjai and J. Y. Park, *Nano Lett.*, 2012, **12**, 5761–5768.
- 28 Z. J. Wu, E. J. Zhao, H. P. Xiang, X. F. Hao, X. J. Liu and J. Meng, *Phys. Rev. B: Condens. Matter Mater. Phys.*, 2007, **76**, 054115.
- 29 K. Albe, K. Nordlund and R. S. Averback, *Phys. Rev. B: Condens. Matter Mater. Phys.*, 2002, **65**, 195124.
- 30 S. Ono, T. Kikegawa and Y. Ohishi, *Solid State Commun.*, 2005, **133**, 55–59.
- 31 N. Seriani, F. Mittendorfer and G. Kresse, *J. Chem. Phys.*, 2010, **132**, 024711.
- 32 Z. Zhao, L. Cui, L.-M. Wang, B. Xu, Z. Liu, D. Yu, J. He, X.-F. Zhou, H.-T. Wang and Y. Tian, *Cryst. Growth Des.*, 2010, **10**, 5024–5026.
- 33 A. Hecq, T. Robert, M. Hecq, J. P. Delrue, J. J. Pireaux and R. Caudano, *J. Less-Common Met.*, 1981, **80**, P83–P89.
- 34 K. H. Westmacott, U. Dahmen and M. J. Witcomb, *Metall. Trans. A*, 1986, **17**, 807–814.